Journal of Wind Engineering & Industrial Aerodynamics 210 (2021) 104536

Contents lists available at ScienceDirect

Journal of Wind Engineering & Industrial Aerodynamics

journal homepage: www.elsevier.com/locate/jweia

Numerical study on wake galloping of tandem circular cylinders considering the effects of mass and spacing ratios

Tian Li [a,b], Takeshi Ishihara [b,*]

[a] School of Civil Engineering, Chongqing University, Chongqing, 400044, China
[b] Department of Civil Engineering, School of Engineering, The University of Tokyo, Tokyo, 113-8656, Japan

ARTICLE INFO

Keywords:
Tandem circular cylinders
LES turbulence Model
Mass ratio
Spacing ratio
Helical wires
Critical velocity of wake galloping

ABSTRACT

The mass and spacing ratios of parallel circular cylinder structures change over a wide range in engineering applications. In this study, the effects of mass ratio, spacing ratio and helical wires on the wake galloping of tandem circular cylinders are investigated by LES turbulence model at the subcritical Reynolds number regime. The upstream cylinder is fixed and the downstream one is free to respond in the transverse direction. The characteristics of wake galloping of tandem circular cylinders are systematically studied for the cases of mass ratios $m^* = 1.8$, 200 and spacing ratios $x_0/D = 4$, 8 and 12. A critical velocity of wake galloping is derived as a function of mass ratio and lift coefficient slope using a wake-stiffness-based model. The suppression of wake galloping by the 4-start helical wires is examined and the maximum amplitude of vibration is found to decrease by 63% because of the positive added damping generated by helical wires.

1. Introduction

The phenomena of flow-induced vibration of circular cylinders are often of primary concern in bridge engineering, offshore industry, aerospace, power transmission, energy extraction, and many other engineering applications, which greatly affect the safety and fatigue life time of structures. For the isolated cylinder, the vortex-induced vibration (VIV) happens when the structural natural frequency f_n approaches the vortex-shedding frequency f_v. It is well known that the vortex-shedding frequency f_v of a fixed isolated circular cylinder follows the rule of Strouhal number $S_t = f_vD/U$ being about 0.2, where U and D are the inflow velocity and diameter of circular cylinder respectively, thus the critical velocity for the VIV of circular cylinder in the reduced scale U_c/f_nD is about 5. Actually, the VIV of circular cylinder happens over a range of reduced velocity $U_r = U/f_nD$ near 5 because the vortex shedding frequency f_v is locked in the structural natural frequency f_n in the resonant regime. Comprehensive reviews on the VIV of circular cylinder are given in Sarpkaya (2004), Williamson and Govardhan (2008) and Bearman (2011).

When a circular cylinder is located in the wake of another circular cylinder, the fluid force on it changes with the spacing between the two cylinders and significant vibrations may be induced. If the downstream cylinder is located in the wake interference region of the upstream one, there is a regime of wake-induced vibration that the vibration amplitude increases with the reduced velocity and this regime is called wake galloping particularly because of its similarity to the classic galloping. It should be mentioned that the wake galloping occurs even for the single-degree-of-freedom (SDOF) system and is distinguished with flutter which involves at least two degrees of freedom (Bokaian and Geoola, 1984). The wake-induced vibration of circular cylinders is more complicated compared with the VIV of an isolated cylinder because of the interference effect and various arrangements of the cylinders. A circular cylinder freely vibrating in the wake of another fixed tandem cylinder of equal diameter acts as a fundamental setting for this issue (Bokaian and Geoola, 1984; Hover and Triantafyllou, 2001; Assi et al., 2010). The formula of the non-dimensionalized vibration amplitude A/D of the downstream circular cylinder is given by applying dimensional analysis to the primary variables as (Assi et al., 2010)

$$\frac{A}{D} = f\left(\mathrm{Re}, U_r, \frac{x_0}{D}, m^*, \zeta\right) \tag{1}$$

where Re is the Reynolds number defined as $\rho UD/\mu$ with ρ and μ standing for the density and dynamic viscosity of fluid respectively. The spacing x_0 is defined as the streamwise center-to-center distance between two cylinders and x_0/D is the streamwise spacing ratio. The mass ratio $m^* = m/(\pi\rho D^2L/4)$ is the ratio of the structure mass to the mass of the displaced fluid, where m and L are the mass and length of the structure respectively. The damping ratio is defined as $\zeta = c/(2m\omega_n)$, where c and ω_n are the damping and the natural angular frequency of the structure.

* Corresponding author.
E-mail address: ishihara@bridge.t.u-tokyo.ac.jp (T. Ishihara).

https://doi.org/10.1016/j.jweia.2021.104536
Received 22 June 2020; Received in revised form 16 January 2021; Accepted 17 January 2021

To investigate the characteristics of wake-induced vibration of tandem circular cylinders, much research was conducted in the last decades. The great part of research was performed by water tank experiments. Bokaian and Geoola (1984) performed water tank test for tandem circular cylinders of $m^* = 6.74$, $\zeta = 0.0144$ and $x_0/D = 1.1$–5 with U_r up to 31. They found that the wake-induced vibration includes two regimes, namely the resonant regime and the galloping regime. In the resonant regime, the cylinder only vibrates at the resonant velocity similar to the VIV of isolated cylinder, while in the galloping regime the cylinder vibrates significantly over a wide range of velocity. These two regimes may be combined or separated depending on the spacing ratio x_0/D. The combined type was found to happen at $x_0/D = 1.5$, the separated type occurred at $x_0/D = 2$–3, and the individual resonant regime was observed at $x_0/D = 4$–5. Hover and Triantafyllou (2001) conducted the water tank test for tandem circular cylinders of $m^* = 3$, $\zeta = 0.04$ and $x_0/D = 4.75$ with U_r up to 18 and they only found the galloping regime. Assi et al. (2006), Korkischko and Meneghini (2010) and Chaplin and Batten (2014) got similar results and only the galloping regime was observed in their water tank test for tandem circular cylinders with small mass ratio m^* and $x_0/D = 2$–6. Assi et al. (2010) preformed a comprehensive research for tandem circular cylinders with $m^* = 2.6$, $\zeta = 0.007$ and $x_0/D = 4$–20 for U_r up to 32. They observed the galloping regime for $x_0/D = 4$–8 and the resonant regime for $x_0/D > 10$.

On the other hand, only a small number of experiments were performed for the structures in the air by wind tunnel experiments where the mass ratios of structures are generally much larger than those in the water by more than 2 orders of magnitude. Kim et al. (2009) investigated the wake-induced vibration of circular cylinders by wind tunnel tests with $m^*\zeta = 0.65$ and U_r up to 12. They found the galloping regime for $x_0/D < 1.3$ and the resonant regime for $x_0/D = 1.3$–4.2 over this limited range of U_r. Yagi et al. (2015) did the wind tunnel test for circular cylinders with $m^* = 553$ and found significant vibration occurred at $U_r = 178$ for $x_0/D = 3$–10. By summarizing the previous experimental results, it is found the regimes of wake-induced vibration of tandem circular cylinders change with the mass and spacing ratios of cylinders and these effects have not been fully clarified so far.

Furthermore, the instability condition of wake-induced vibration of circular cylinders was also investigated by some theoretical researches. Simpson (1971) established a model to estimate the instability condition for the downstream cylinder by the quasi-steady theory. Paidoussis and Price (1988) proposed two kinds of mechanisms to explain the wake-induced vibration of the downstream cylinder. One is the damping-controlled mechanism, which is similar to the mechanism of classic galloping, and the other is the stiffness-controlled mechanism, which is named as the wake-induced flutter. It should be noted that some researchers also used the terminology "wake-induced galloping'' to describe the latter mechanism (Simiu and Scanlan, 1996). Price and Piperni (1988) found that the critical velocity of the wake-induced vibration of circular cylinders could not be effectively reduced by increasing the structural damping based on their analytical model. This implies that the stiffness-controlled mechanism may be the right one for the wake-induced vibration. However, the analytical model of the wake-induced flutter is developed only for the two-degree-of-freedom (2DOF) system and failed to explain the wake galloping of circular cylinders in the SDOF system. More recently, Assi et al. (2013) proposed the concept of wake stiffness and performed a series of experiments for tandem circular cylinders with different structural stiffness. They found that the wake stiffness not only sustained the oscillatory motion, but also dominated the overall stiffness of the system. Until now, the roles of damping and stiffness for the critical velocity of wake galloping are still controversial.

Despite the critical condition, the vibration amplitude of wake galloping is also important for engineering application considering the maintenance cost of structures. Various mechanical, aerodynamic or hydrodynamic dampers are used to suppression the vibration of circular cylinders (Zdravkovich, 1981). Among them, the helical wires are thought as a fluid dynamic damping equipment and they are superior to the mechanical damper in terms of the scope of application especially for the risers of offshore platforms and bridge cables, even though their effectiveness is not unconditional and often limited in the Reynolds number range as the observation of Weaver (1959). Ishihara and Li (2020) studied the effect of helical wires on the suppression of VIV for an isolated circular cylinder. They found the maximum amplitude of VIV was decreased by helical wires due to the enhancement of the three-dimensionality of flow in the spanwise direction and the generation of positive aerodynamic damping. Korkischko and Meneghini (2010) investigated the effect of helical strakes with sharp edges on the suppression of VIV and wake galloping of circular cylinders. They found the VIV was almost suppressed by helical strakes and the wake galloping was significantly reduced even though the helical strakes were attached on only the downstream cylinder. The performance of helical wires to suppress the wake galloping of tandem circular cylinders has not been investigated yet before.

In the recent years, the computational resource and technology are developing rapidly and the numerical simulation is used as an efficient tool to investigate the fluid-structure interaction. It provides simultaneous flow patterns, fluid forces and dynamic responses, and allows a coupled analysis of the fluid-structure interaction. However, most of previous numerical studies on the wake-induced vibration of tandem circular cylinders were performed at the low Reynolds number by the two-dimensional simulations (Bao et al., 2011; Carmo et al., 2011; Han et al., 2014; Mysa et al., 2016; Li et al., 2018; Yao and Jaiman, 2019), and only resonant regimes were observed in their simulations. On the other hand, the galloping regime was reproduced by the three-dimensional simulations. Mysa et al. (2017) investigated the wake galloping of tandem circular cylinders with $m^* = 2.6$, $\zeta = 0.007$ and $x_0/D = 4$ at $\mathrm{Re} = 5000$–10000 using large eddy simulations (LES) and showed good agreement with the experimental data. Nguyen et al. (2018) studied the wake galloping of tandem circular cylinders with $m^* = 2.6$, $\zeta = 0.007$, $x_0/D = 5$ and 8 at $\mathrm{Re} = 3 \times 10^4$ using detached eddy simulations (DES) and also reproduced the experiment results. Currently, the three-dimensional numerical studies for the wake galloping of tandem circular cylinder with high Reynolds numbers are still limited and almost all of them focused on the structures with low mass ratios. More numerical researches are expected to be performed for the wake galloping of tandem circular cylinders with high mass ratios. Additionally, more comprehensive analysis for the key parameters and critical condition of wake galloping of circular cylinders should be carried out through numerical simulations.

In this study, the wake galloping of tandem circular cylinders is investigated by LES turbulence model over a range of mass and spacing ratios. The numerical model used in this research is introduced in Section 2. The accuracy of this numerical model is validated by the experimental data, and the effects of mass and spacing ratios on the wake galloping of circular cylinders are investigated in Section 3. An analytical model of the critical velocity of wake galloping is derived by a wake-stiffness-based model and is used to explain the effect of mass and spacing ratios on the wake galloping of tandem circular cylinders qualitatively in Section 4. The suppression of wake galloping of tandem circular cylinders by helical wires is studied and its mechanism is explained in Section 5. The conclusions are summarized in Section 6.

2. Numerical model

The numerical model used in this study is explained in this section. The governing equations and solution schemes are given in Section 2.1. The computational domain and numerical mesh are introduced in Section 2.2. The modelling of oscillation system is shown in Section 2.3.

2.1. Governing equations and schemes

The governing equations for the flow are the unsteady incompressible Navier-Stokes equations with LES turbulence model, which are derived

by filtering continuity and Navier-Stokes equations in a moving mesh system as

$$\frac{\partial \rho \tilde{u}_i}{\partial x_i} = 0 \tag{2}$$

$$\rho \frac{\partial \tilde{u}_i}{\partial t} + \rho \frac{\partial \tilde{u}_i}{\partial x_j}\left(\tilde{u}_j - \hat{u}_j\right) = -\frac{\partial \tilde{p}}{\partial x_i} + \mu \frac{\partial}{\partial x_j}\left(\frac{\partial \tilde{u}_i}{\partial x_j} + \frac{\partial \tilde{u}_j}{\partial x_i}\right) - \frac{\partial \tau_{ij}}{\partial x_j} \tag{3}$$

where x is the coordinate, u is the velocity, p is the pressure and t is the time. The subscripts i and j stand for different directions in Cartesian coordinates, which include the streamwise, spanwise and transverse directions. The "~" denotes the filtered component and $\hat{u}$ is the velocity component of the moving mesh. τ_{ij} is the subgrid-scale stress defined by

$$\tau_{ij} = \rho\widetilde{u_i u_j} - \rho \tilde{u}_i \tilde{u}_j \tag{4}$$

The subgrid-scale stresses resulting from the filtering operations are unknown, and they are modelled as

$$\tau_{ij} = -2\mu_t \tilde{S}_{ij} + \frac{1}{3}\tau_{kk}\delta_{ij} \tag{5}$$

where μ_t is the subgrid-scale turbulent viscosity, and δ_{ij} is the Kronecker delta. $\tilde{S}_{ij}$ is the rate-of-strain tensor, i.e. the symmetric component of the velocity gradient tensor $\nabla\tilde{u}$ for the resolved scale defined as

$$\tilde{S}_{ij} = \frac{1}{2}\left(\frac{\partial \tilde{u}_i}{\partial x_j} + \frac{\partial \tilde{u}_j}{\partial x_i}\right) \tag{6}$$

The dynamic Smagorinsky-Lilly model (Smagorinsky, 1963; Germano et al., 1991; Lilly, 1992) is used to model the subgrid-scale turbulent viscosity μ_t as

$$\mu_t = \rho L_s^2 |\tilde{S}| = \rho L_s^2 \sqrt{2\tilde{S}_{ij}\tilde{S}_{ij}} \tag{7}$$

where $|\tilde{S}| = \sqrt{2\tilde{S}_{ij}\tilde{S}_{ij}}$ and L_s is the mixing length of subgrid-scales defined as

$$L_s = \min\left(\kappa d, C_s V^{\frac{1}{3}}\right) \tag{8}$$

where κ is the von Karman constant and is taken equal to 0.42. C_s is Smagorinsky constant, which is dynamically computed based on the information provided by the resolved scales of motion (ANSYS Inc, 2015). d is the distance to the closest wall, and V is the volume of a computational cell.

For the wall-adjacent cells, when they are in the laminar sub-layer, the wall shear stress is obtained from the laminar stress-strain relationship as

$$\frac{\tilde{u}}{u_\tau} = \frac{\rho u_\tau y^*}{\mu} \tag{9}$$

where $\tilde{u}$ is the filtered velocity that is tangential to the wall; u_τ is the friction velocity; y^* is the distance between the center of the cell and the wall. If the mesh cannot resolve the laminar sub-layer, it is assumed that the centroid of the wall-adjacent cells falls within the logarithmic region of the boundary layer, and the law-of-the-wall is employed as

$$\frac{\tilde{u}}{u_\tau} = \frac{1}{\kappa}\ln E\left(\frac{\rho u_\tau y^*}{\mu}\right) \tag{10}$$

where the constant E is taken equal to 9.8.

The filtered Navier-Stokes equations are solved with the commercial CFD code ANSYS Fluent 16.2 (ANSYS Inc, 2015) using the control volume method. The second-order central difference scheme is used for the convective and viscosity terms, and the second-order implicit scheme is used for the unsteady term. SIMPLE (Semi-Implicit Method for Pressure Linked Equations) algorithm is employed for solving the discretized equations (Patankar, 1980). The simulations were performed on the parallel computing cluster system in the Bridge and Wind Engineering Laboratory of the University of Tokyo (Intel Xeon CPU E5-2667 v4, 240 cores, 960 GB memory). The simulation with 80 cores takes about 150 h for each reduced velocity.

2.2. Computational domain and mesh

In this study, a pair of circular cylinders in a tandem arrangement is focused and the center-to-center direction is along with the flow streamwise. The spacing ratio x_0/D between two cylinders ranges from 4 to 12. The width and depth of computational domain as shown in Fig. 1 are $50D + x_0$ and $30D$ respectively. The spanwise length of the domain in this paper was $4D$, referred to the previous numerical study of VIV of isolated circular cylinder by Ishihara and Li (2020) that this length is enough to simulate the correlation length of circular cylinder in the spanwise direction. The upstream cylinder is located $15D$ downstream of the inlet, which is always fixed. The downstream cylinder can move transversely under the effect of fluid force. Uniform velocity condition is specified at the inlet boundary, and zero diffusive condition is used at the outlet boundary. Symmetric condition is used for the top, bottom and transverse surfaces of the domain.

The mesh of entire computational domain and an enlarged view of the mesh in the vicinity cylinder is shown in Fig. 2. Hexahedron mesh is used with high resolution near the cylinder to capture the flow accurately. There is an interface in the center of these two cylinders. For the unsteady analysis where the downstream cylinder is subjected to oscillations, the sliding mesh technique is employed at the interface to allow oscillations. The left side of interface is fixed while the right side can move transversely, combining with dynamic laying mesh technique used in the transverse boundary.

An enlarged view of the mesh in the vicinity of helical wires is shown in Fig. 3. The helical wires are attached on both upstream and downstream circular cylinders and are arranged as 4-start pattern with a pitch ratio of $p/D = 8$ and a diameter ratio of $d/D = 0.1$, which are effective for the VIV suppression according to the study of Ishihara and Li (2020). Since the helical wire is much smaller in size compared to the cylinder section, it requires a high resolution to capture the flow accurately. The wedge mesh is employed around the wire connected with hexahedron mesh around the other parts around the circular cylinder to ensure the numerical accuracy in the region close to the complex geometry of helical wires. A hybrid mesh system is used and divided into several zones. The inner mesh is formed by sweeping the two-dimensional mesh in the spanwise direction and twisting the mesh at the same time, which builds the helical pattern for the wires. The outer mesh is swept along the spanwise direction rigidly. The twisted inner mesh around cylinder is connect with the outer mesh using a non-matching interface shown as a red circle. The mesh sizes of both sides of the interface are similar, thus

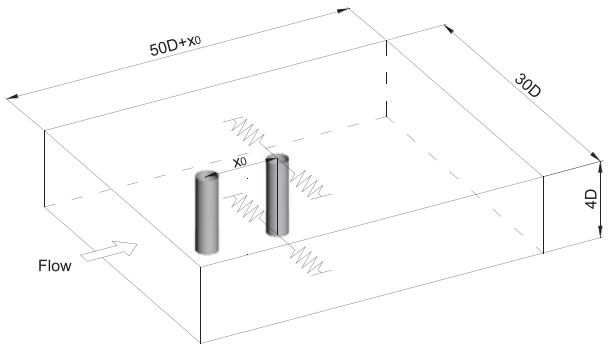

Fig. 1. Overview of computational domain.

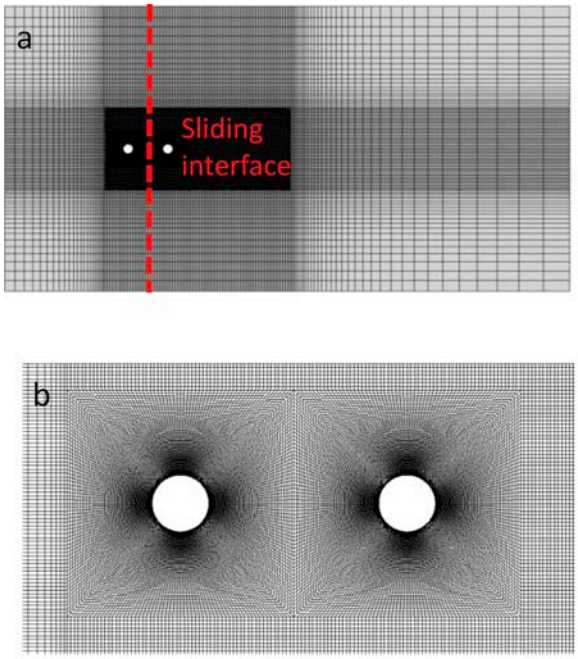

Fig. 2. Mesh of (a) entire computational domain and (b) around cylinders.

the accuracy can be kept. This mesh system not only helps to generate a reasonable mesh, but also allows less quantity of mesh to speed up the calculation with sufficient accuracy. These mesh system and numerical condition have been proved successful to simulate the VIV of isolated cylinder with and without helical wires and the details can be found in Ishihara and Li (2020).

The convergence of mesh is tested through several non-dimensional fluid force coefficients of the bare and wired cylinders for the case of $x_0/D = 4$, namely the drag and lift coefficients as well as the Strouhal number. The drag and lift coefficients are defined as C_D=F_D/(0.5$\rho U^2 DL$) and C_L=F_L/(0.5$\rho U^2 DL$), where F_D and F_L are the drag and lift forces obtained by integrating pressure and friction over the cylinder surface. The cylinder diameter D used to calculate fluid force coefficients is kept as the diameter of the bare cylinder even when the helical wires are attached.

The frequency of vortex shedding f_v to calculate the Strouhal number S_t is obtained by the spectrum analysis of lift force on cylinders. The mean drag coefficient $C_{D\ mean}$, the root mean square of lift coefficient $C_{L\ rms}$ and the Strouhal number S_t predicted by meshes with different resolutions are shown in Table 1 for Re = 10,000. The subscripts *1* and *2* stand for the upstream and downstream cylinder respectively. The mesh resolution is increased gradually from Mesh 1 to Mesh 3 for the bare and wired cylinders respectively. The changes of results are shown in brackets. It is noticed that the difference of numerical results between Mesh 2 and Mesh 3 is less than 4% for both bare and wired cylinders, which is acceptable for the requirement of convergence in engineering applications. Thus, Mesh 2 is used in the following simulations in consideration of both accuracy and efficiency.

2.3. Modelling of oscillatory motion

As the upstream cylinder is relatively stable and the downstream one mainly vibrates in the transverse direction for the tandem circular cylinders (Yagi et al., 2015), the upstream cylinder is fixed and the downstream cylinder is simplified as a SDOF system which can freely vibrate in the transverse direction in this research. The structural flexibility of the downstream cylinder can be modelled by using a mass-damping-spring system in the transverse direction as

$$m\ddot{y} + c\dot{y} + ky = F_L(t) \tag{11}$$

where y is the transverse displacement of cylinder, k is the structural stiffness and $F_L(t)$ is the transient lift force acting on the cylinder. To analyze the structural response of this SDOF system, the equation of motion is solved using the fourth-order Runge-Kutta method.

The sliding mesh is used to update the dynamic domain during the simulation. It is a special case of the general dynamic mesh wherein the nodes move rigidly in a given dynamic mesh zone. Additionally, multiple cells are connected with each other through non-conformal interfaces. As the mesh motion is updated in time, the non-conformal interfaces are likewise updated to reflect the new position of each zone. The flux across the non-conformal interfaces is estimated considering the two adjoining cells that move relative to each other as shown in Fig. 4. For example, to compute the flux across the interface into cell V, newly formed faces c-d and d-e are used to compute the required parameters from cells I and II (Sarwar and Ishihara, 2010). The accuracy of sliding mesh is found higher than other dynamic mesh methods, such as the remeshing

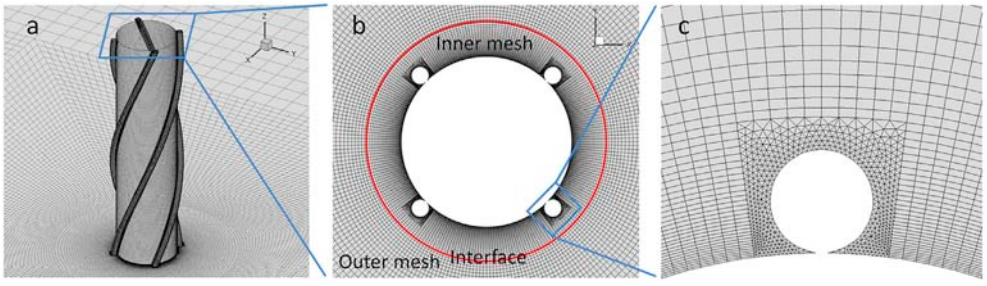

Fig. 3. Mesh near the wired cylinder: (a) bird view; (b) top view; (c) view of the mesh near wires.

Table 1
Mesh convergence test.

	Mesh quantity	$C_{D\ mean\ 1}$	$C_{D\ mean\ 2}$	$C_{L\ rms\ 2}$	$S_{t\ 2}$
Bare cylinder-Mesh 1	2,514,000	1.234	0.458	0.87	0.168
Bare cylinder-Mesh 2	3,352,000	1.185 (3.97%)	0.435 (5.02%)	0.875 (0.57%)	0.178 (5.95%)
Bare cylinder-Mesh 3	4,614,000	1.176 (0.76%)	0.431 (0.92%)	0.872 (0.34%)	0.181 (1.66%)
Wired cylinder-Mesh 1	2,918,160	1.129	−0.0483	0.169	0.128
Wired cylinder-Mesh 2	3,890,880	1.132 (0.27%)	−0.0531 (9.94%)	0.186 (10.05%)	0.133 (3.90%)
Wired cylinder-Mesh 3	5,152,880	1.131 (0.09%)	−0.0510 (3.95%)	0.193 (3.76%)	0.132 (0.75%)

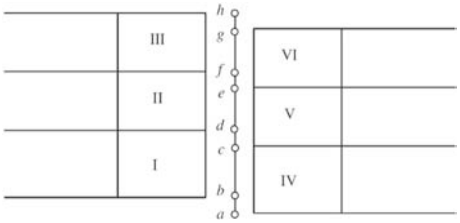

Fig. 4. Sliding interface between adjacent cells.

method, for the large-amplitude motion of mesh (Ferziger and Peric, 2002).

3. Numerical results

The numerical results for the fixed and free-vibration cases are validated by comparing with the experiment data in Section 3.1. The effects of mass and spacing ratios on the wake galloping of tandem circular cylinders are illustrated in Sections 3.2 and 3.3 respectively.

3.1. Validation of numerical model

The fluid force on the downstream cylinder varies with the location of cylinder due to the wake of the upstream cylinder. The distribution of mean pressure coefficient $C_{p\ mean}$ and mean lift coefficient $C_{L\ mean}$ on the fixed downstream cylinder with $x_0/D = 4$ and $y_0/D = 0$, 0.5 and 1 are predicted by numerical simulations, where y_0 is the transverse distance between the two cylinders. The pressure coefficient is defined as $C_p=(p-p_{ref})/(0.5\rho U^2)$, where p is the pressure at the sampling point and p_{ref} is the reference pressure in the undisturbed flow. The schematic of the parallel cylinders is shown in Fig. 5 and the simulated results are compared with the experimental data of Yagi (2003) in Figs. 6 and 7, where θ is the angle of point on the surface of cylinder and $\theta = 0^\circ$ corresponds to the flow-stagnation point on the frontal surface. The Reynolds number in numerical simulation is kept same with experiment as Re = 23,000. The predicted mean pressure coefficients $C_{p\ mean}$ and mean lift coefficient $C_{L\ mean}$ on the downstream cylinder agree well with the experiment. It can be found that the $C_{L\ mean}$ always points to the position $y_0/D = 0$ and acts as a restoring force when the downstream cylinder leaves the centerline of wake of the upstream cylinder as shown in Fig. 7. The reason is that the negative pressure on the downstream cylinder has a larger magnitude for the side near to the centerline than the other side as shown in Fig. 6.

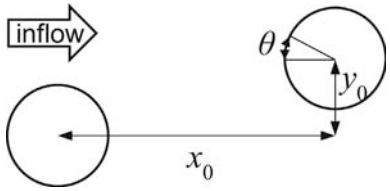

Fig. 5. Schematic of parallel cylinders.

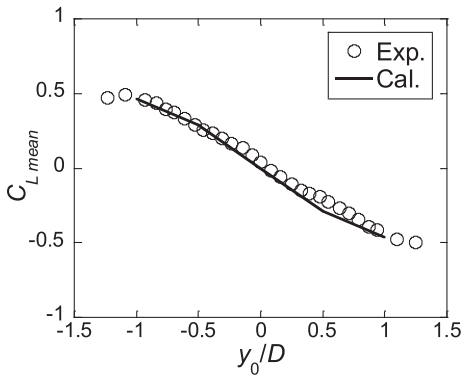

Fig. 7. Variation of the mean lift coefficients with the transverse position.

The flow pattern in the gap between the two fixed cylinders with the spacing ratio $x_0/D = 4$ is found to change with the Reynolds number (Ljungkrona and Sundén, 1993; Zhou et al., 2009). When Re < 7000–9000, the shed shear flow from the upstream cylinder always attaches the downstream cylinder, which is called the reattached pattern.

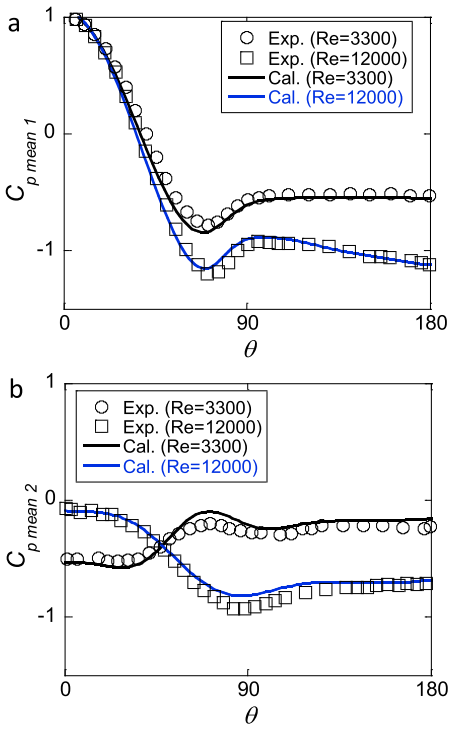

Fig. 8. Pressure distribution on cylinders with different Reynolds numbers on (a) upstream cylinder and (b) downstream cylinder.

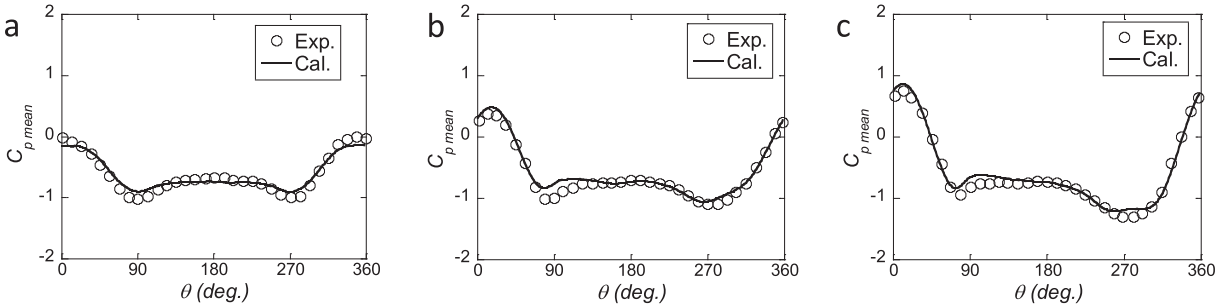

Fig. 6. Comparison of predicted and measured pressure distributions on the downstream cylinder at (a) $y_0/D = 0$, (b) $y_0/D = 0.5$ and (c) $y_0/D = 1$.

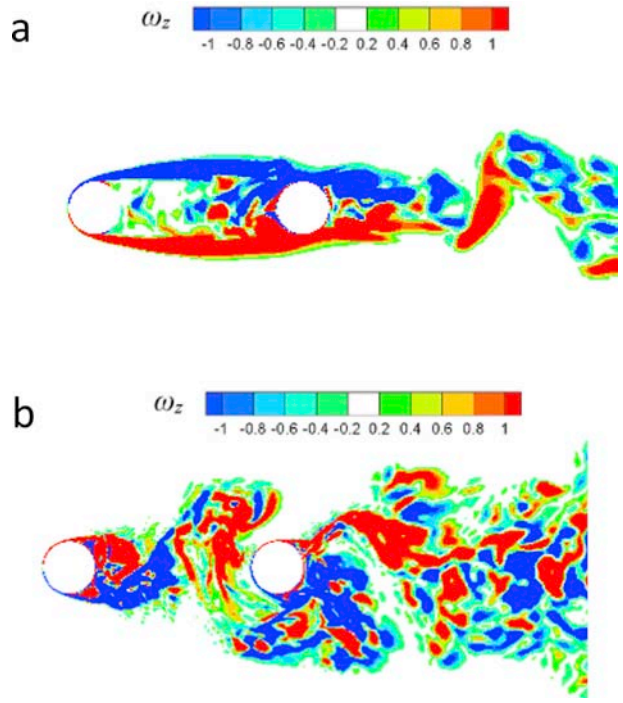

Fig. 9. Vorticity around tandem circular cylinders at (a) Re = 3300 and (b) Re = 12,000.

When Re > 7000–9000, the vortex shedding will be formed between the two cylinders, which is called the co-shedding vortex pattern. The pressure distributions of Re = 3300 and 12,000 are simulated to represent the results of these different patterns, and the numerical results agree well with the experimental ones of Ljungkrona and Sundén (1993) as shown in Fig. 8. The flow patterns around cylinders for different Re are visualized by the non-dimensional spanwise vorticity ω_z in the central plane of $z/D = 2$ as shown in Fig. 9 and also agree with the experiment results of Ljungkrona and Sundén (1993), where the non-dimensional spanwise vorticity is defined as $\omega_z=(\partial u_2/\partial x_1-\partial u_1/\partial x_2)/(U/D)$.

The predicted and measured amplitude and frequency of free-vibration are compared with the experimental data of Korkischko and Meneghini (2010) with the spacing ratio $x_0/D = 4$. The structural parameters are same with the experiment, where the mass ratio m^* is 1.8 and the damping ratio in the vacuo ζ is 0.0045. The variation of non-dimensionalized amplitude A/D with the reduced velocity U_r are used to describe the vibration. It should be noticed that the reduced velocity is non-dimensionalized by the structural natural frequency f_n in the water in Korkischko and Meneghini (2010) and by that in the vacuo here. The free vibrations with the reduced velocity U_r changing from 3 to 17 are simulated. Both f_n and D are fixed, while the inflow velocity U is varied in these simulations, resulting in Re = 2400–9600 which is same with the experimental condition. The oscillation under each U_r is simulated over 30 periods to get stable statistics, and the amplitudes of vibration A are determined by taking the average of 10% highest peaks in the time series of the displacement response for each case which is same as the experiment. The time series of the cylinder displacement at U_r = 12.6 is shown in Fig. 10 for instance.

The predicted non-dimensional vibration amplitudes A/D and ratios of vibration frequency f_o to structural natural frequency f_n are shown in Fig. 11. The numerical results are denoted by filled circles and the experimental data are expressed as solid lines. A small step of reduced velocity U_r was used in the experiments, while a larger step is used in the numerical simulations because the numerical simulation takes much longer time to obtain a data compared with the experiment. It is noticed that the amplitude of vibration of the downstream cylinder increases as the reduced velocity U_r increases and shows a typical phenomenon of

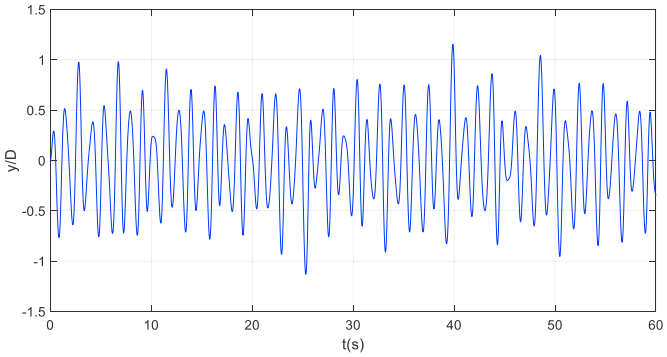

Fig. 10. A time series of the cylinder displacement at U_r = 12.6.

wake galloping. The vibration frequency f_o identified by the displacement spectrum is close to the structural natural frequency f_n at the low reduced velocity and slightly increases as U_r increases. The numerical results favorably agree with the experimental data for the wake galloping of tandem circular cylinders.

3.2. Effect of mass ratio

The wake galloping of tandem circular cylinders in the water with small mass ratio $m^* = 1.8$ is experimentally investigated by Korkischko and Meneghini (2010). However, the mass ratios of structure in the air are generally much larger than those in the water by more than 2 orders of magnitude. The wake galloping of the downstream cylinder with a large mass ratio is always encountered in the wind engineering applications, such as the bridge cables and transmission lines. The free-vibration simulations are performed to investigate the effect of mass ratio on the wake galloping of tandem circular cylinders. The vibration of the downstream cylinder is simulated with $\zeta = 0.0005$ and $m^* = 200$ which is about 100 times of the value used in Korkischko and Meneghini (2010). The reduced velocity U_r up to 100 is considered to catch the resonant and galloping regimes of wake-induced vibration. The case of $m^* = 1.8$ is also simulated with this wider range of reduced velocities for comparison. The Re is kept to 10,000 for the case of $m^* = 200$ to avoid the Reynolds number effect and increases with U_r for the case of $m^* = 1.8$ with a max value of 58,000. The predicted amplitude and frequency of vibration for the case of $x_0/D = 4$ are shown in Fig. 12. The resonant regime happens over a range of U_r = 3–10 for the cylinder of $m^* = 200$, which is same as the VIV of isolated cylinder (Ishihara and Li, 2020). However, the amplitude of vibration decreases after the resonant regime and increases again from $U_r = 20$ to 100, resulting in separated resonant and galloping regimes, which is distinguished with the case of $m^* = 1.8$. The critical velocity of wake galloping in the case of $m^* = 200$ is much larger than that in the case of $m^* = 1.8$. The frequency of vibration f_o for the downstream cylinder of $m^* = 1.8$ increases significantly as the reduced velocity U_r increases, while that in the case of $m^* = 200$ is always close to the natural frequency of structure f_n. It is because the effect of the added mass is much more significant for the cylinder with smaller mass ratio m^* (Assi et al., 2013).

Fig. 13 illustrates the mean drag coefficient $C_{D\ mean}$ and the fluctuating lift coefficient $C_{L\ rms}$ of the downstream cylinders. The numerical results of those parameters for the isolated cylinder from Ishihara and Li (2020) are also plotted for comparison. It can be seen that the $C_{D\ mean}$ is generally smaller than that of the isolated cylinder due to the wake effect of the upstream cylinder. The $C_{L\ rms}$ for the case of $m^* = 1.8$ is close to that of the isolated cylinder except for the resonant regime, while the $C_{L\ rms}$ for the case of $m^* = 200$ is higher than that of the isolated cylinder. The magnitude of $C_{D\ mean}$ and $C_{L\ rms}$ significantly increase at the resonant velocity $U_r = 7$ which shows obvious features of the resonant regime. They keep almost constant for $U_r > 20$ for both cases of $m^* = 1.8$ and 200

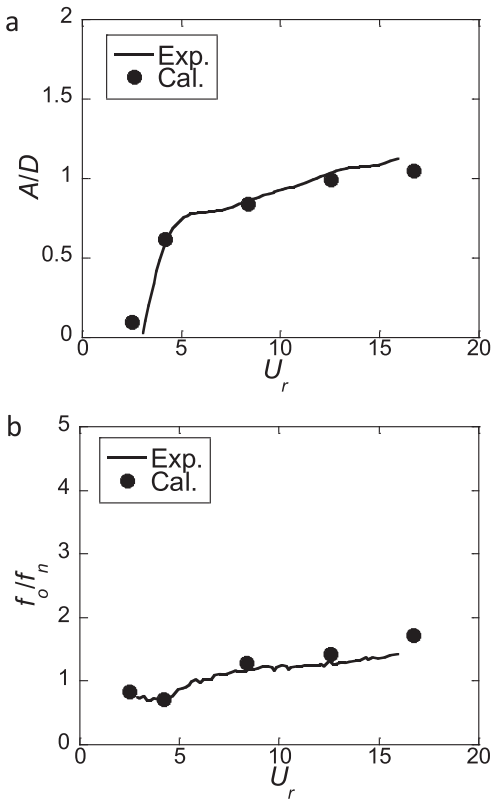

Fig. 11. Comparison of predicted and measured (a) amplitudes and (b) frequencies of free vibration for the downstream cylinder with $m^* = 1.8$ and $x_0/D = 4$.

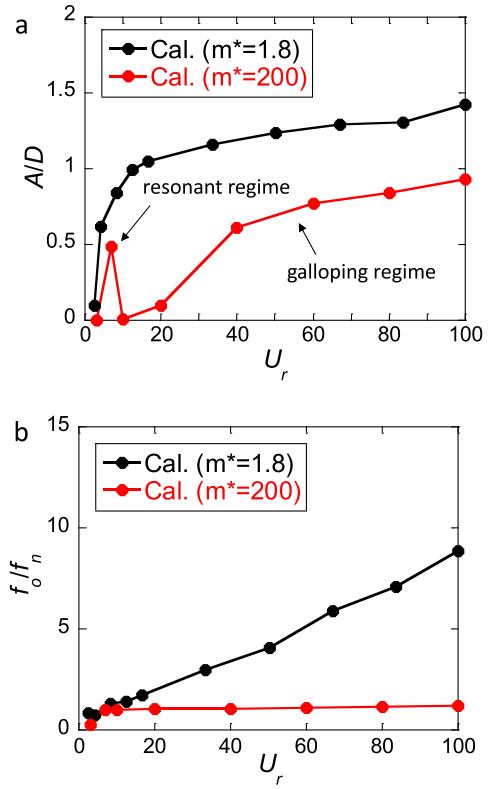

Fig. 12. Influence of mass ratio on (a) vibration amplitudes and (b) vibration frequencies of the downstream cylinders with $x_0/D = 4$.

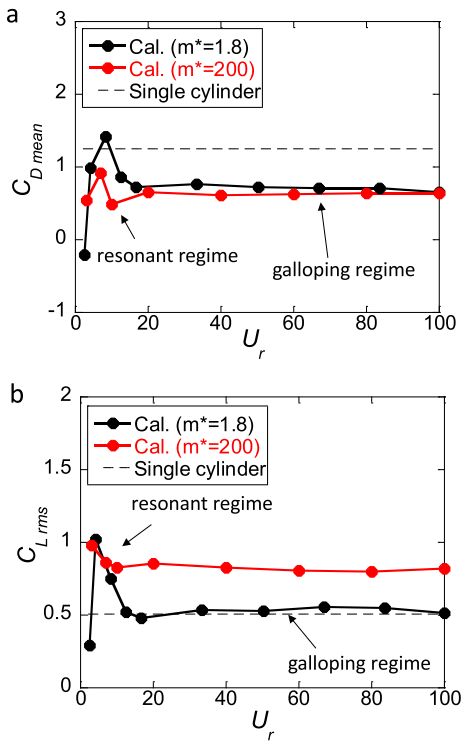

Fig. 13. Fluid force coefficients on the downstream cylinders with $x_0/D = 4$: (a) drag coefficients; (b) lift coefficients.

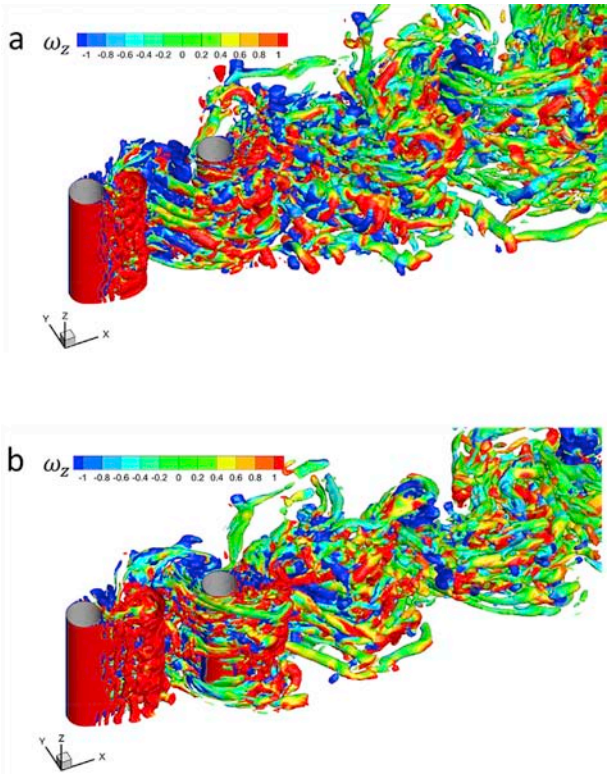

Fig. 14. Bird views of vortex core identified by the iso-surface of $e_2 = -0.2$ around two cylinders with $x_0/D = 4$ at $U_r = 100$ for (a) $m^* = 1.8$ and (b) $m^* = 200$.

which belongs to the galloping regime. It indicates that the resonant regime exists not only in the case of $m^* = 200$ but also in the case of $m^* = 1.8$. The resonant and galloping regimes are combined in the case of $m^* = 1.8$ but separated in the case of $m^* = 200$.

Bird views of vortex core around the cylinders for both cases of $m^* = 1.8$ and 200 with $x_0/D = 4$ at $U_r = 100$ are visualized in Fig. 14 by the iso-surfaces of the non-dimensional second negative eigenvalue e_2 of the tensor $\tilde{S}^2 + \tilde{\Omega}^2$ using the method proposed by Jeong and Hussain (1995). $e_2 = \lambda_2/(U/D)^2$ is set as -0.2 with λ_2 being the dimensional second negative eigenvalue of the tensor $\tilde{S}^2 + \tilde{\Omega}^2$. $\tilde{S}$ and $\tilde{\Omega}$ are the symmetric and antisymmetric components of the velocity-gradient tensor $\nabla\tilde{u}$. $\tilde{S}_{ij}$ is defined in Eq. (6) and $\tilde{\Omega}_{ij}$ is expressed as

$$\tilde{\Omega}_{ij} = \frac{1}{2}\left(\frac{\partial \tilde{u}_i}{\partial x_j} - \frac{\partial \tilde{u}_j}{\partial x_i}\right) \tag{12}$$

These iso-surfaces are colored by the non-dimensional spanwise vorticity ω_z. It is noticed that the vortices shed from the upstream cylinder are relatively two-dimensional while the wake of the downstream cylinder has strong three-dimensionality. The contours of instantaneous non-dimensional spanwise vorticity ω_z in the central plane of $z/D = 2$ at different phases in a cycle of oscillation at $U_r = 100$ are shown in Fig. 15 for both cases of $m^* = 1.8$ and 200. It can be seen the co-shedding vortex pattern forms for both cases at this velocity. The excursion of the wake in the case of $m^* = 1.8$ is more significant than that in the case of $m^* = 200$ because of the larger lateral motion of the downstream cylinders in the case of $m^* = 200$.

The spectra of lift coefficient C_L of two cylinders at $U_r = 100$ for both cases of $m^* = 1.8$ and 200 are shown in Fig. 16 to illustrate the features of lift force, where the subscripts *1* and *2* stand for the upstream and downstream cylinders respectively. The normalized spectrum $SU/\sigma^2 D$ and the normalized frequency fD/U are used, where f is the frequency, S and σ are the spectrum and standard deviation of C_L respectively. It is found for both cases of $m^* = 1.8$ and 200, the lift coefficient spectra of the upstream cylinder include peaks at $S_t \approx 0.18$, which are close to the vortex shedding frequency of an isolated fixed cylinder. The lift

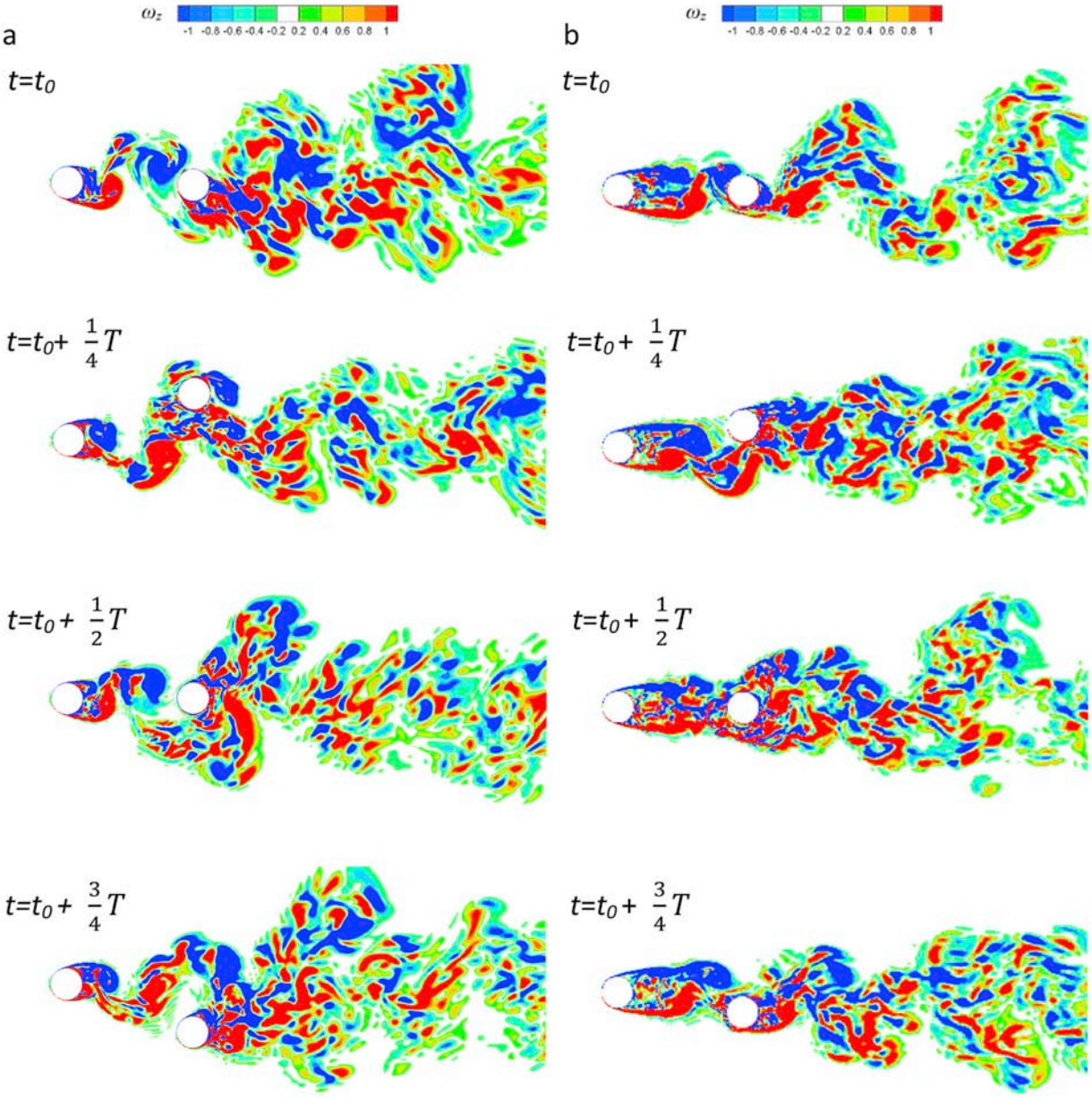

Fig. 15. Vorticity around two cylinders with $x_0/D = 4$ at $U_r = 100$ for (a) $m^* = 1.8$ and (b) $m^* = 200$.

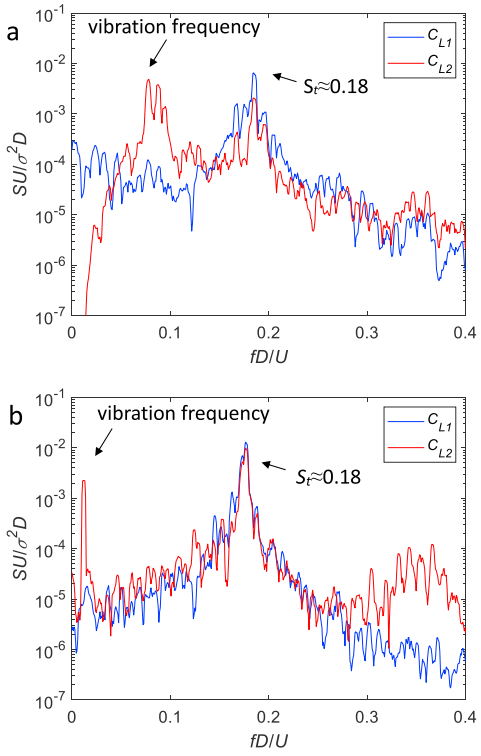

Fig. 16. Spectra of lift coefficient of two cylinders with $x_0/D = 4$ at $U_r = 100$ for (a) $m^* = 1.8$ and (b) $m^* = 200$.

coefficient spectra of the downstream cylinder include two peaks, one is consistent with the vibration frequency and the other is at $S_t \approx 0.18$. The peak at the vibration frequency dominates for the case of $m^* = 1.8$ due to the large lateral motion of the downstream cylinder, while the peak at $S_t \approx 0.18$ is more significant for the case of $m^* = 200$ because of the small lateral motion of the downstream cylinder.

3.3. Effect of spacing ratio

The effect of spacing ratio on the wake galloping has been studied by Assi et al. (2010) for tandem circular cylinders with small mass ratio $m^* = 2.6$. The resonant regime is found to combine with the galloping regime for $x_0/D = 4$–8, and only resonant regime occurs for $x_0/D = 10$–20. However, the effect of spacing ratio on the wake galloping of tandem cylinders with large mass ratio m^* has not been studied experimentally or numerically before, so that the wake galloping with a large mass ratio of $m^* = 200$ and damping ratio of $\zeta = 0.0005$ is investigated for three spacing ratios of $x_0/D = 4$, 8 and 12 over a wide range of U_r in this study. The numerical results of vibration amplitudes are shown in Fig. 17. It is found that all three cases show the separated resonant regime at $U_r = 3$–10 and galloping regime. The critical velocity of wake galloping increases and the vibration amplitude A/D of wake galloping decreases as x_0/D increases. The vibration frequency f_o is always close to the structural natural frequency f_n for the cases with large mass ratio m^*, so that the numerical results for that are neglected.

The mean drag coefficients $C_{D\ mean}$ and fluctuating lift coefficients $C_{L\ rms}$ of the downstream circular cylinder with different spacing ratio x_0/D are shown in Fig. 18. The numerical results of those parameters for the isolated circular cylinder from Ishihara and Li (2020) are also plotted for comparison. It is shown that the distributions of $C_{D\ mean}$ and $C_{L\ rms}$ for $x_0/D = 4$, 8 and 12 are similar, which always have peaks in the resonant regime and keeps almost constant in the galloping regime. The values of $C_{D\ mean}$ are close for different x_0/D and are always smaller than that of the isolated cylinder due to the wake effect of the upstream cylinder. The $C_{L\ rms}$ decreases with the increase of x_0/D. The values of $C_{L\ rms}$ at the

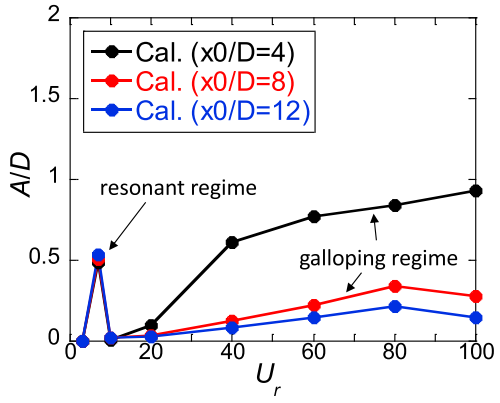

Fig. 17. Effects of spacing ratio on the vibration amplitudes of downstream cylinder with $m^* = 200$.

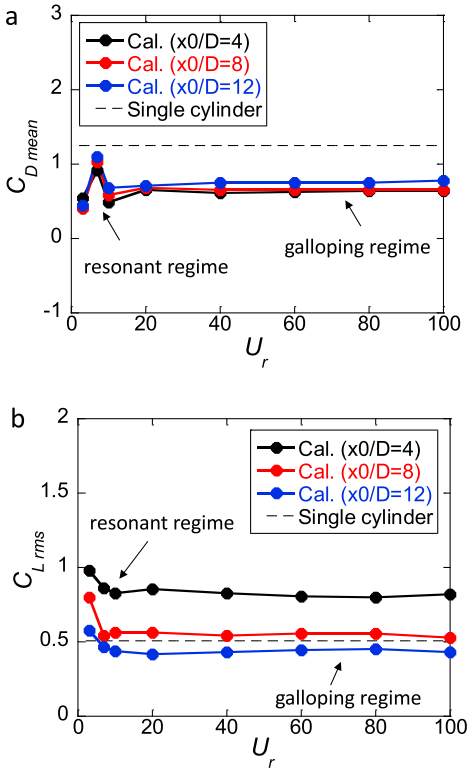

Fig. 18. Fluid force coefficients of the downstream cylinders with $m^* = 200$: (a) drag coefficients; (b) lift coefficients.

galloping regime with $x_0/D = 8$ and 12 are close to that of the isolated cylinder.

The patterns of non-dimensional spanwise vorticity ω_z in the central plane of $z/D = 2$ at different phases in a cycle of oscillation for the cases of $x_0/D = 8$ and 12 with $m^* = 200$ at $U_r = 100$ are shown in Fig. 19. It is found the wakes of the upstream cylinders are well developed and similar to the wake of isolated cylinder, while the wakes of downstream cylinders are more turbulent. The excursion of the wake is not significant because of the small lateral motion of the downstream cylinder.

The spectra of lift coefficient of two cylinders with $m^* = 200$ at $U_r = 100$ for both cases of $x_0/D = 8$ and 12 are shown in Fig. 20 to illustrate the features of lift force. It is found for both cases of $x_0/D = 8$ and 12, the lift coefficient spectra of the upstream cylinder include peaks at Strouhal number $S_t \approx 0.2$, which is close to the vortex shedding frequency of an isolated fixed cylinder and that in the cases of $x_0/D = 4$. For the case of

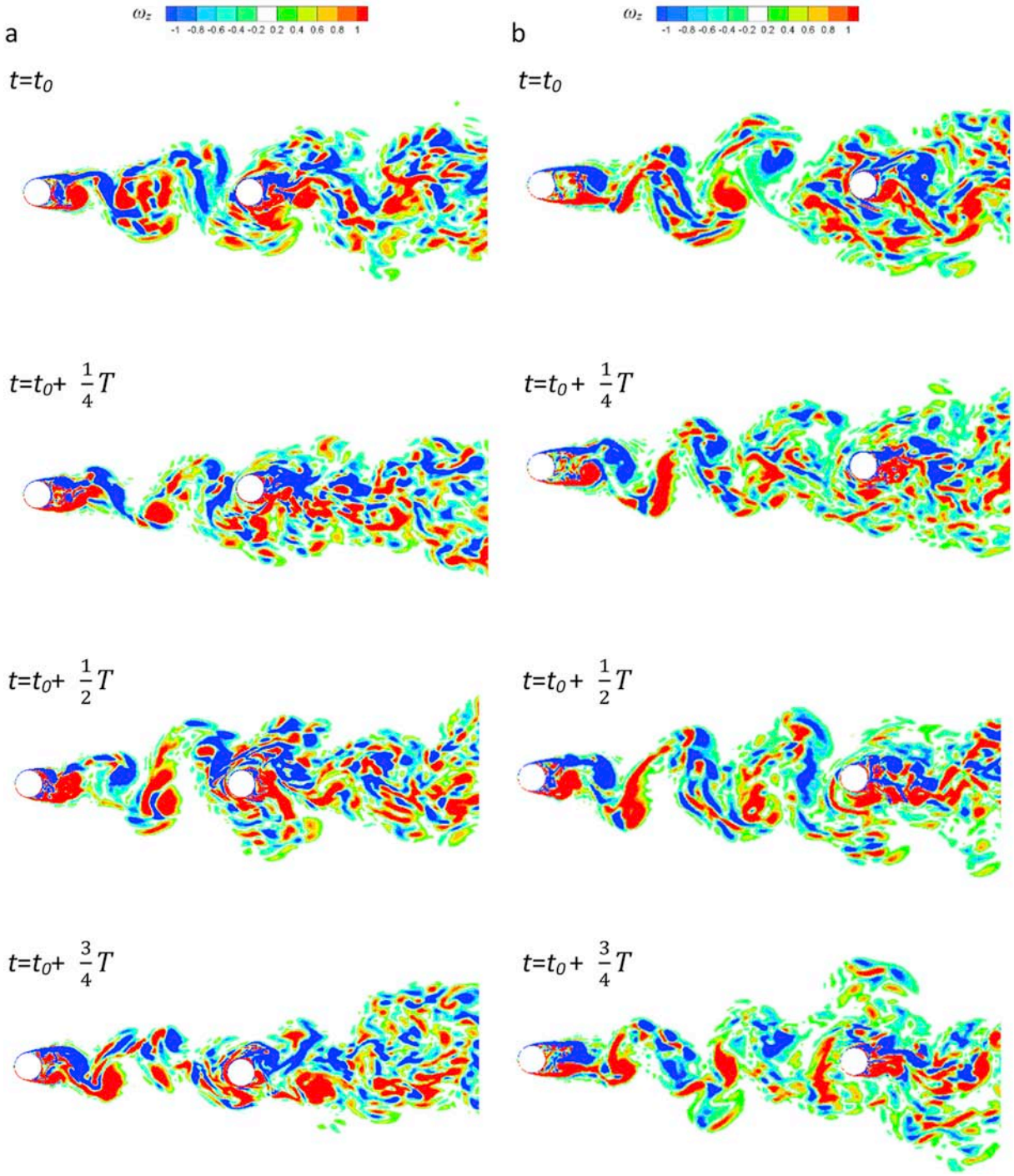

Fig. 19. Vorticity around two cylinders with $m^* = 200$ at $U_r = 100$ for (a) $x_0/D = 8$ and (b) $x_0/D = 12$.

$x_0/D = 8$, the lift coefficient spectrum of the downstream cylinder includes three peaks that one is consistent with the vibration frequency and the other two peaks are at $S_t \approx 0.15$ and 0.2. The peak at the vibration frequency is not significant because of the small lateral motion of the downstream cylinder. For the case of $x_0/D = 12$, the peak at the vibration frequency disappears due to the weak vibration of the downstream cylinder and the other two peaks at $S_t \approx 0.15$ and 0.2 remain.

To examine the features of flow behind the two cylinders, the correlation coefficient R_i of the streamwise velocity u at couples of points symmetrically across the wake at $y_i/D = \pm 0.6$ is investigated and defined as

$$R_i = \frac{\sum_{t_1}^{t_2}(u_{ai} - \overline{u_{ai}})(u_{bi} - \overline{u_{bi}})}{\left(\left(\sum_{t_1}^{t_2}(u_{ai} - \overline{u_{ai}})^2\right)\left(\sum_{t_1}^{t_2}(u_{bi} - \overline{u_{bi}})^2\right)\right)^{0.5}} \tag{13}$$

where the subscripts a_i and b_i stand for the points at $y_i = 0.6D$ and $y_i = -0.6D$ respectively. The subscripts $i = 1$ and 2 stands for the points behind the upstream and downstream cylinders respectively. Fig. 21 shows the schematic of the locations of the couples of points behind the two cylinders. The streamwise distances from the centers of upstream and downstream cylinders to the points are donated as x_1 and x_2 respectively. The results of R_i in the case of $m^* = 200$ and $x_0/D = 12$ at $U_r = 100$ are shown in Fig. 22, where R_1 and R_2 stand for the correlation

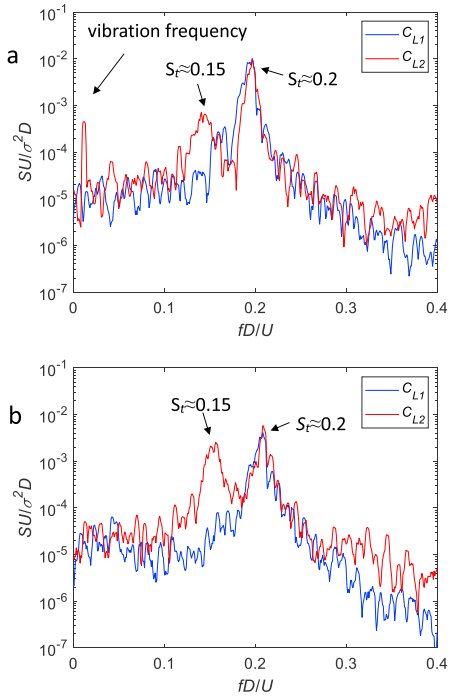

Fig. 20. Spectra of lift coefficient of two cylinders with $m^* = 200$ at $U_r = 100$ for (a) $x_0/D = 8$ and (b) $x_0/D = 12$.

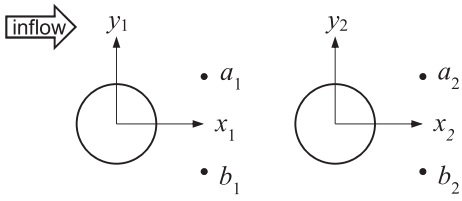

Fig. 21. Schematic of the locations of the couples of points behind the two cylinders.

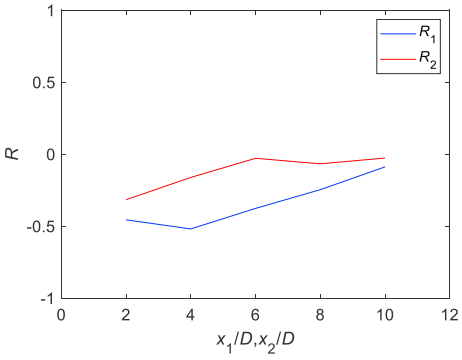

Fig. 22. Variation of the correlation coefficient of streamwise velocity u with the streamwise distances x_1 and x_2 at couples of points at $y_i/D = \pm 0.6$ for the case of $x_0/D = 12$.

coefficients at the points behind the upstream and downstream cylinders respectively. It is found the streamwise velocities at the couple of points close to the cylinders are negatively correlated and the magnitudes of correlation coefficients decrease as the streamwise distance x_1 and x_2 increase. For the same streamwise distance $x_1 = x_2$, the negative correlation of the streamwise velocities at the locations behind the upstream cylinder is stronger than that behind the downstream cylinder and is

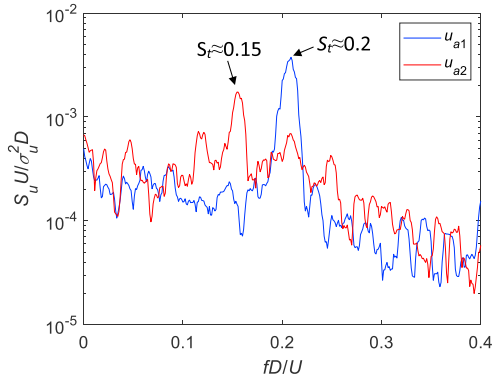

Fig. 23. The spectra of streamwise velocity u_{a1} at the point ($x_1/D = 2$, $y_1/D = 0.6$) and u_{a2} at the point ($x_2/D = 2$, $y_2/D = 0.6$) for the case of $x_0/D = 12$.

more similar to the features of the Karman vortex shedding. In addition, the spectra of streamwise velocity u_{a1} at the point ($x_1/D = 2$, $y_1/D = 0.6$) and u_{a2} at the point ($x_2/D = 2$, $y_2/D = 0.6$) are plotted in Fig. 23. The normalized spectrum S_uU/σ_u^2D and the normalized frequency fD/U are used, where S_u and σ_u are the spectrum and standard deviation of streamwise velocity u respectively. It is found that the Strouhal number S_t of vortex shedding from the upstream cylinder is about 0.2 and that from the downstream cylinder is about 0.15, which correspond to the two peaks at $S_t \approx 0.2$ and 0.15 in the spectra of the lift coefficients C_L of the downstream cylinder for the cases with $x_0/D = 8$ and 12 as shown in Fig. 20. The peak of the spectra of u_{a1} at $S_t \approx 0.2$ is more significant and dominating than that of u_{a2} at $S_t \approx 0.15$, which indicates the periodicity of vortex shedding from the upstream cylinder is stronger than that from the downstream cylinder.

4. Discussion on the critical velocity of wake galloping with an analytical model

The effects of mass and spacing ratios on the wake galloping of tandem circular cylinders have been studied in the previous sections, and the mechanism of these effect is discussed by an analytical model in this section. The analytical model of the critical velocity of wake galloping of tandem circular cylinders is derived using the concept of wake stiffness in Section 4.1. The effects of mass and spacing ratios on the wake galloping of tandem circular cylinders are then explained in Section 4.2 through this model.

4.1. Analytical model of the critical velocity of wake galloping

As shown by Li et al. (2018) and Ishihara and Li (2020), the fluid dynamic force on the vibrating cylinder can be decomposed into two components as

$$m\ddot{y} + c\dot{y} + ky = F_L(t) = F_b(t) + F_u(t, y, \dot{y}, \ddot{y}) \tag{14}$$

where the terms on the right-hand-side are the buffeting force F_b and the unsteady fluid force F_u, which is a function of time t, displacement y, velocity $\dot{y}$ and acceleration $\ddot{y}$. The unsteady fluid force F_u can be separated into two terms based on the orthogonality of displacement (or acceleration) and velocity. The force F_k related with the displacement y and the acceleration $\ddot{y}$ is called the in-phase force. The force F_c related with the velocity $\dot{y}$ is called the out-of-phase force. They are expressed as

$$F_u(t, y, \dot{y}, \ddot{y}) = F_k(t, y, \ddot{y}) + F_c(t, \dot{y}) \tag{15}$$

The in-phase and out-of-phase forces may be assumed as the linear functions of displacement and its derivative. The two terms on the right-hand-side of Eq. (15) are then expressed as

$$F_k(t, y, \ddot{y}) = -k_a y \tag{16}$$

$$F_c(t,\dot{y}) = -c_a\dot{y} \tag{17}$$

where k_a and c_a are called the added stiffness and the added damping respectively since they lead to a change in the total mass and damping of the system. Eq. (14) is rewritten as

$$m\ddot{y} + (c+c_a)\dot{y} + (k+k_a)y = F_b(t) \tag{18}$$

The added stiffness and damping can be calculated based on the orthogonality of displacement and velocity as

$$k_a = -\frac{\int_0^T F_L(t)y(t)dt}{\int_0^T y(t)^2 dt} \tag{19}$$

$$c_a = -\frac{\int_0^T F_L(t)\dot{y}(t)dt}{\int_0^T \dot{y}(t)^2 dt} \tag{20}$$

The displacement and lift force of a cylinder under vibration can be expressed by the harmonic formula as presented by Parkinson (1971), Williamson and Govardhan (2004) and Assi et al. (2010) as

$$y = A\sin(\omega t) \tag{21}$$

$$F_L = \frac{1}{2}\rho U^2 DL\widehat{C}_L \sin(\omega t + \phi) \tag{22}$$

where $\widehat{C}_L$ is the amplitude of lift coefficient and ϕ is the phase delay between the transverse force and the displacement of cylinder.

Based on the quasi-steady theory, the amplitude of lift coefficient $\widehat{C}_L$ equals to the mean lift coefficient $C_{L\ mean}$ of the fixed downstream cylinder at the transverse position equaling the vibration amplitude. It is noticed that the mean lift coefficient $C_{L\ mean}$ has a linear behavior between $-0.5 < y_0/D < 0.5$ for $x_0/D = 4$ as shown in Fig. 7. Thus, the amplitude of lift coefficient $\widehat{C}_L$ is supposed by

$$\widehat{C}_L = -\alpha\frac{A}{D} \tag{23}$$

where α is a positive constant value and $-\alpha$ is the slope of $C_{L\ mean}$ to y_0/D. Assi et al. (2013) defined this effect as the wake stiffness because the lift force on the downstream cylinder is a linear function of transverse position and acts as a restoring force in the system. It should be noticed that the linear relationship between $C_{L\ mean}$ and A/D is a valid approximation at small-amplitude vibrations and can be used to predict the critical velocity of the wake galloping. The nonlinearities of $C_{L\ mean}$ with A/D appear at large-amplitude vibrations and should be considered to analyze the features of wake galloping at high reduced velocities.

By combining Eqs. (19)–(23), the added stiffness and damping can be derived as

$$k_a = \frac{1}{2}\rho U^2 L\alpha\cos(\phi) \tag{24}$$

$$c_a = \frac{1}{2\omega}\rho U^2 L\alpha\sin(\phi) \tag{25}$$

It is found that the magnitude of added stiffness k_a and added damping c_a increase with the inflow velocity U, the magnitude of lift coefficient slope α and cosine/sine of phase lag ϕ.

The phase lag ϕ changes from 0° to 180° in the resonant regime as shown in Fig. 24, which was also found in the experiment by Assi et al. (2010) for the case of $m^* = 2.6$. Thus, the added stiffness changes to a negative value after the resonant regime and the added damping is close to null except in the resonant regime. After the resonant regime, the magnitude of negative added stiffness increases and the total system stiffness $k_a + k$ decreases as the inflow velocity U increases. The inflow velocity U researches a critical value when $k_a = -k$ and the total stiffness

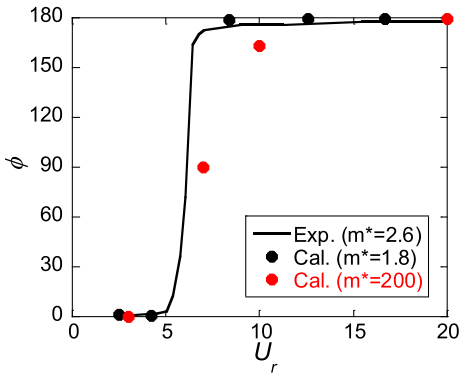

Fig. 24. Phase lag between lift force and displacement of the downstream cylinders.

of system becomes zero, then the system tends to diverge and the amplitude of vibration increases significantly. A critical velocity of wake galloping U_c is defined at this condition and results in

$$k - \frac{1}{2}\rho U_c^2 L\alpha = m\omega_n^2 - \frac{1}{2}\rho U_c^2 L\alpha = 0 \tag{26}$$

The critical velocity of wake galloping in the reduced scale is then derived as

$$\frac{U_c}{f_n D} = \sqrt{\frac{2\pi^3}{\alpha}m^*} \tag{27}$$

4.2. Discussion on the effects of mass and spacing ratios

The characteristics of wake galloping of tandem circular cylinder with different mass and spacing ratios are investigated by numerical simulations in Section 3. The critical velocity of wake galloping is found to increase with the mass and spacing ratios, which has not been explained by any analytical model before to the authors' knowledge. The effects of mass and spacing ratios on the critical velocity of wake galloping are explained qualitatively by the proposed analytical mode in Eq. (27) for the first time. It shows that the critical velocity of wake galloping increases linearly with $\sqrt{m^*}$ and decreases linearly with $\sqrt{\alpha}$. The variation of amplitude A/D with the reduced velocity U_r divided by $\sqrt{m^*}$ for the cases with the different mass ratios for the case of $x_0/D = 4$ is shown in Fig. 25. It can be seen the galloping regime of wake galloping happens at close values of $U_r/\sqrt{m^*}$. It is indicated that the combination and separation of resonant and galloping regimes are mainly caused by the effect of mass ratio on the critical velocity of wake galloping.

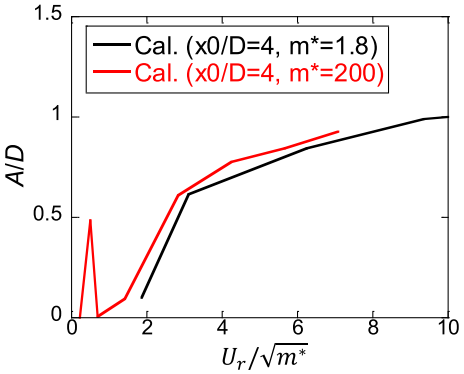

Fig. 25. The variation of vibration amplitude of the downstream cylinders with $U_r/\sqrt{m^*}$.

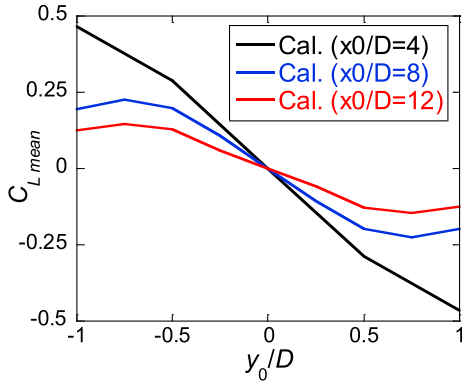

Fig. 26. Mean lift coefficient of the downstream cylinders at different transverse position.

The effect of spacing ratio on the critical velocity of wake galloping is caused by the change of the magnitude of lift coefficient slope α. The mean lift coefficients for $x_0/D = 4$, 8 and 12 and $y_0/D = -1 \sim 1$ are shown in Fig. 26. It can be seen that as x_0/D increases the magnitude of lift coefficient slope α decreases and the linear relationship of y_0/D and $C_{L\ mean}$ exists over a narrower range for $x_0/D = 8$ and 12 than that of $x_0/D = 4$. Fig. 27 shows the variation of vibration amplitude A/D with $U_r\sqrt{\alpha}$. It is found the wake galloping starts from the close positions with different spacing ratios. The nonlinear relationship of y_0/D and $C_{L\ mean}$ for $x_0/D = 8$ and 12 leads smaller vibration amplitudes than that of $x_0/D = 4$.

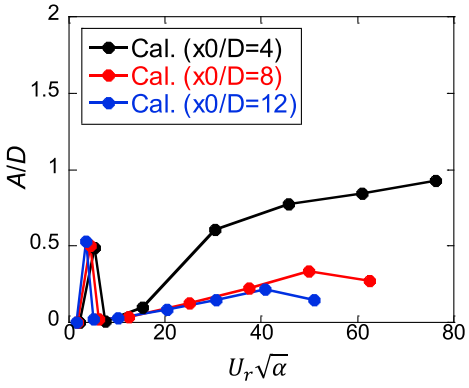

Fig. 27. The variation of vibration amplitude of the downstream cylinders with $U_r\sqrt{\alpha}$.

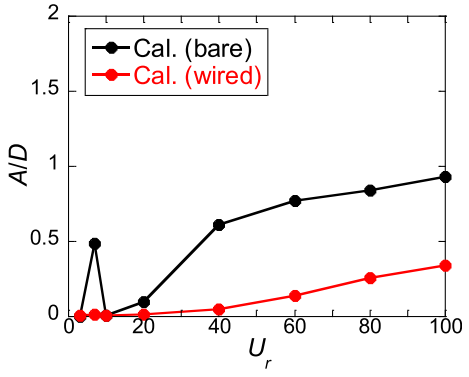

Fig. 28. Comparison of vibration amplitudes of the downstream cylinders with and without helical wires for $m^* = 200$ and $x_0/D = 4$.

5. Discussion on the wake galloping suppression by helical wires

The critical velocity of wake galloping of tandem circular cylinders mainly depends on the system stiffness based on the discussion in Section 4, while the vibration amplitude of wake galloping of tandem circular cylinders is found to relate with the system damping (Kubo et al., 2012). The helical wires are used as a fluid dynamic damping equipment to suppress the wake galloping of circular cylinders. The vibration amplitudes of the downstream cylinders with and without helical wires for $m^* = 200$ and $x_0/D = 4$ are shown in Fig. 28. It is found that the helical wires successfully suppress the wake galloping. The maximum amplitude of vibration at the reduced velocity $U_r = 100$ is reduced by 63%. The vibration frequency f_o is always close to the structural natural frequency f_n and the numerical results for that are neglected.

The predicted mean drag coefficient $C_{D\ mean}$ and fluctuating lift force $C_{L\ rms}$ of the downstream cylinders with and without helical wires for $m^* = 200$ and $x_0/D = 4$ are shown in Fig. 29. The $C_{D\ mean}$ and $C_{L\ rms}$ of the wired cylinder slightly increase as U_r increases and are smaller than those of the bare cylinder. The reduction of $C_{L\ rms}$ of the wired cylinder was also mentioned by Ishihara and Li (2020) for the cases of fixed and free-vibrating isolated cylinders.

The non-dimensional spanwise vorticity ω_z in the central plane of $z/D = 2$ at different phases in a cycle of oscillation for the case of $m^* = 200$ and $x_0/D = 4$ at $U_r = 100$ are shown in Fig. 30. It is found the flows on the upper and lower sides of the upstream cylinder directly attach the downstream cylinder and do not form vortex pairs as that of the bare cylinders shown in Figs. 14 and 15. The near wake of the downstream cylinder is destroyed by the helical wires and the Karman vortex street forms far away from the downstream cylinder. It is similar to the wake of isolated cylinder with helical wires as shown by Ishihara and Li (2020).

The helical wires are always regarded as a fluid dynamic damping device in engineering application so that the vibration-induced added damping is identified to clarify the effect of helical wires on the suppression of wake galloping through the forced vibration numerical

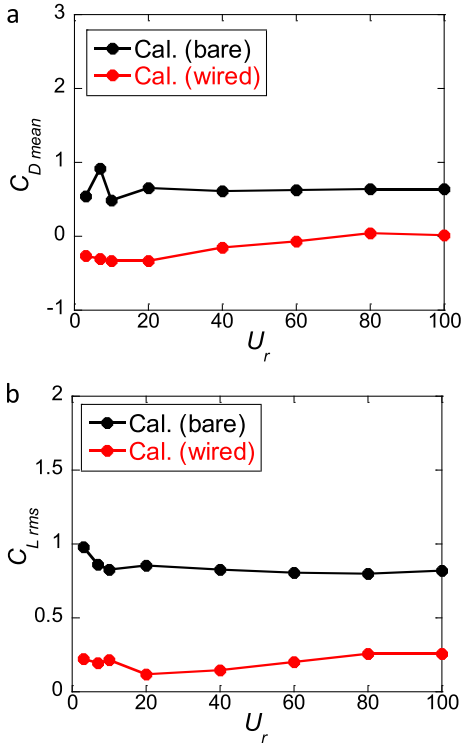

Fig. 29. Comparison of (a) mean drag coefficients and (b) fluctuating lift coefficients of the downstream cylinders with and without helical wires for $m^* = 200$ and $x_0/D = 4$.

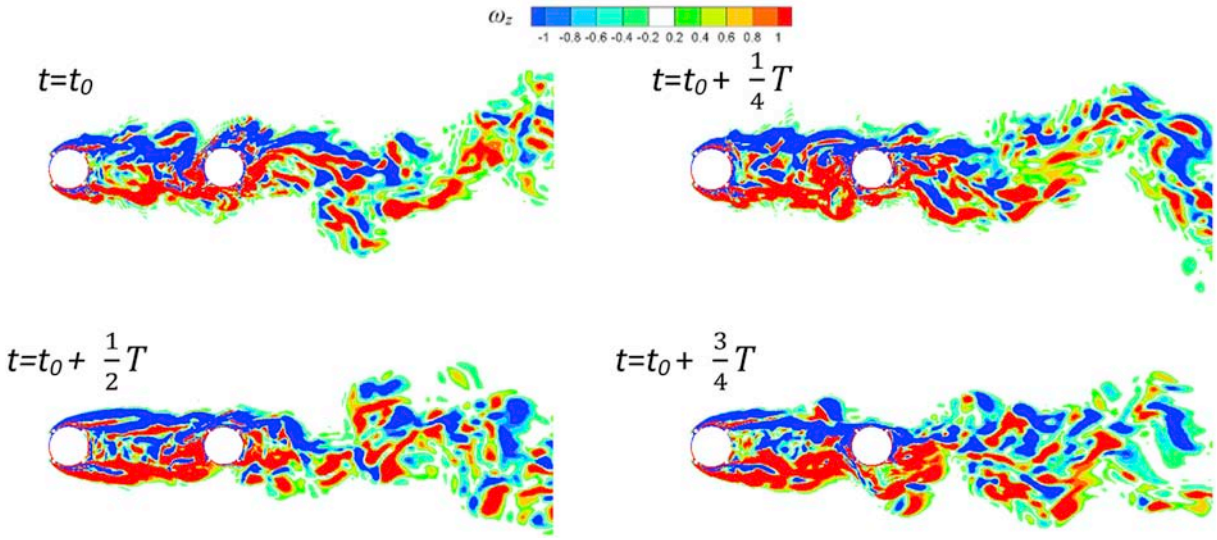

Fig. 30. Vorticity around tandem circular cylinders with helical wires for $m^* = 200$ and $x_0/D = 4$ at $U_r = 100$.

simulation. In the simulation, the upstream cylinder is fixed and the downstream cylinder is oscillated sinusoidally as

$$y = A\sin(2\pi f_n t) \tag{28}$$

where A is the oscillating amplitude and is set as $0.5D$, which is a small value compared with the maximum vibration amplitude of bare cylinders of about $1.0D$. This forced oscillation amplitude is located in the range of linear relationship of $C_{L\ mean}$ and y_0/D for $x_0/D = 4$ as shown in Fig. 7 and is reasonable to use to get the added damping. The oscillating frequency equals to the natural frequency of cylinder f_n. The added damping is calculated by Eq. (20) and the total damping of system is defined as

$$c_{total} = c + c_a \tag{29}$$

Fig. 31 shows the normalized damping c_{non} for the added, structural and total system damping of the downstream cylinder with and without helical wires at $U_r = 100$, where c_{non} is the damping normalized by the structural damping c. It is found that the added damping for the bare cylinder is negative and leads a negative total damping of system. However, the added damping for the wired cylinder is positive and causes a positive total damping of system. The negative total damping induces the wake galloping for the bare cylinders, while the positive one suppresses the vibration for the wired cylinders. The positive added damping generated by the helical wires has the same effect as found for the VIV suppression of isolated circular cylinder by Ishihara and Li (2020).

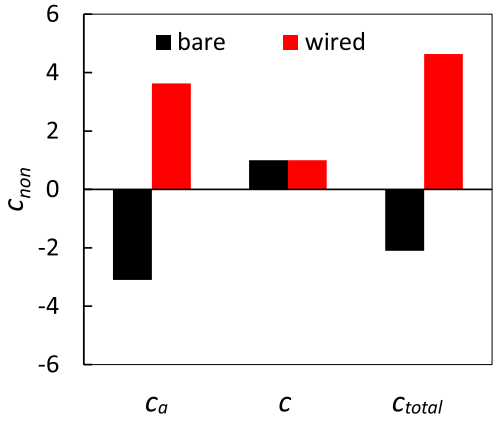

Fig. 31. Normalized added, structural and total damping of the downstream cylinders.

6. Conclusions

The wake galloping of tandem circular cylinders is investigated using LES turbulence model. A numerical model for a transversely free-vibrating circular cylinder in the wake of another fixed cylinder is proposed and the accuracy is validated by comparing with the experimental data. The characteristics of wake galloping and dynamic fluid forces on the downstream cylinder as well as the flow patterns are examined to clarify the effect of mass and spacing ratios. An analytical model of the critical velocity of wake galloping is derived through a wake-stiffness-based model to explain the effects of mass and spacing ratios on the critical velocity of wake galloping. The effect of helical wires on the wake galloping suppression is also investigated. The main conclusions are as follows:

1) The wake-induced vibration of tandem circular cylinders includes two regimes, namely the resonant and galloping regimes. The resonant regime is always located at the reduced velocity of $U_r = 3$–10, while the critical velocity of the galloping regime increases with the mass and spacing ratios. As a result, the resonant and galloping regimes are combined with low mass ratio $m^* = 1.8$ and spacing ratio $x_0/D = 4$, but separated with high mass ratio $m^* = 200$ and spacing ratio $x_0/D = 4$–12.
2) An analytical model for predicting the critical velocity of wake galloping of tandem circular cylinders is derived as a function of mass ratio m^* and the magnitude of lift coefficient slope α using a wake-stiffness-based model and is used to explain the effect of mass and spacing ratios on the wake galloping. The critical velocity of wake galloping increases linearly with $\sqrt{m^*}$ and decreases linearly with $\sqrt{\alpha}$, which is validated by the data of numerical simulation.
3) The 4-start helical wires with a pitch ratio of $p/D = 8$ and a diameter ratio of $d/D = 0.1$ are used to suppress the wake galloping of tandem circular cylinders successfully. The mean drag coefficient $C_{D\ mean}$ and fluctuating lift coefficient $C_{L\ rms}$ are also reduced by helical wires due to their effects on the gap flow and the wake. The positive added damping is generated by helical wires which is the main reason of wake galloping suppression.

CRediT authorship contribution statement

Tian Li: Data curation, Formal analysis, Methodology, Investigation, Software, Validation, Visualization, Writing - original draft, Writing - review & editing. **Takeshi Ishihara:** Conceptualization, Formal analysis,

Funding acquisition, Methodology, Project administration, Resources, Supervision, Writing - review & editing.

Declaration of competing interest

The authors declare that they have no known competing financial interests or personal relationships that could have appeared to influence the work reported in this paper.

Acknowledgements

The authors wish to thank the 111 Project of China (Grant No. B18062) and the China Scholarship Council (CSC201707090062) for the funding support.

References

Ansys Inc, 2015. ANSYS FLUENT 16.2 Theory Guide.
Assi, G.R.S., Meneghini, J.R., Aranha, J.A.P., Bearman, P.W., Casaprima, E., 2006. Experimental investigation of flow-induced vibration interference between two circular cylinders. J. Fluid Struct. 22 (6–7), 819–827.
Assi, G.R.S., Bearman, P.W., Meneghini, J.R., 2010. On the wake-induced vibration of tandem circular cylinders: the vortex interaction excitation mechanism. J. Fluid Mech. 661, 365–401.
Assi, G.R.S., Bearman, P.W., Carmo, B.S., Meneghini, J.R., Sherwin, S.J., Willden, R.H.J., 2013. The role of wake stiffness on the wake-induced vibration of the downstream cylinder of a tandem pair. J. Fluid Mech. 718, 210–245.
Bao, Y., Zhou, D., Tu, J., 2011. Flow interference between a stationary cylinder and an elastically mounted cylinder arranged in proximity. J. Fluid Struct. 27 (8), 1425–1446.
Bearman, P.W., 2011. Circular cylinder wakes and vortex-induced vibrations. J. Fluid Struct. 27 (5–6), 648–658.
Bokaian, A., Geoola, F., 1984. Wake-induced galloping of two interfering circular cylinders. J. Fluid Mech. 146, 383–415.
Carmo, B.S., Sherwin, S.J., Bearman, P.W., Willden, R.H.J., 2011. Flow-induced vibration of a circular cylinder subjected to wake interference at low Reynolds number. J. Fluid Struct. 27 (4), 503–522.
Chaplin, J.R., Batten, W.M.J., 2014. Simultaneous wake-and vortex-induced vibrations of a cylinder with two degrees of freedom in each direction. J. Offshore Mech. Arctic Eng. 136 (3).
Ferziger, J.H., Peric, M., 2002. Computational Methods for Fluid Dynamics. Springer Science and Business Media.
Germano, M., Piomelli, U., Moin, P., Cabot, W.H., 1991. A dynamic subgrid-scale eddy viscosity model. Phys. Fluid. Fluid Dynam. 3 (7), 1760–1765.
Han, Z., Zhou, D., Tu, J., 2014. Wake-induced vibrations of a circular cylinder behind a stationary square cylinder using a semi-implicit characteristic-based split scheme. J. Eng. Mech. 140 (8), 04014059.
Hover, F.S., Triantafyllou, M.S., 2001. Galloping response of a cylinder with upstream wake interference. J. Fluid Struct. 15 (3–4), 503–512.
Ishihara, T., Li, T., 2020. Numerical study on suppression of vortex-induced vibration of circular cylinder by helical wires. J. Wind Eng. Ind. Aerod. 197, 104081.
Jeong, J., Hussain, F., 1995. On the identification of a vortex. J. Fluid Mech. 285, 69–94.
Kim, S., Alam, M.M., Sakamoto, H., Zhou, Y., 2009. Flow-induced vibrations of two circular cylinders in tandem arrangement. Part 1: characteristics of vibration. J. Wind Eng. Ind. Aerod. 97 (5–6), 304–311.
Korkischko, I., Meneghini, J.R., 2010. Experimental investigation of flow-induced vibration on isolated and tandem circular cylinders fitted with strakes. J. Fluid Struct. 26 (4), 611–625.
Kubo, Y., Yuki, Y., Ishii, H., Hatakenaka, S., Kawato, C., 2012. A feature on wake galloping of a bridge in full sized parallel cable model. J. Struct. Eng. 58A, 518–527 (in Japanese).
Li, T., Yang, Q., Ishihara, T., 2018. Unsteady aerodynamic characteristics of long-span roofs under forced excitation. J. Wind Eng. Ind. Aerod. 181, 46–60.
Li, X., Zhang, W., Gao, C., 2018. Proximity-interference wake-induced vibration at subcritical Re: mechanism analysis using a linear dynamic model. Phys. Fluid. 30 (3), 033606.
Lilly, D.K., 1992. A proposed modification of the Germano subgrid scale closure method. Phys. Fluid. Fluid Dynam. 4 (3), 633–635.
Ljungkrona, L., Sundén, B., 1993. Flow visualization and surface pressure measurement on two tubes in an inline arrangement. Exp. Therm. Fluid Sci. 6 (1), 15–27.
Mysa, R.C., Kaboudian, A., Jaiman, R.K., 2016. On the origin of wake-induced vibration in two tandem circular cylinders at low Reynolds number. J. Fluid Struct. 61, 76–98.
Mysa, R.C., Law, Y.Z., Jaiman, R.K., 2017. Interaction dynamics of upstream vortex with vibrating tandem circular cylinder at subcritical Reynolds number. J. Fluid Struct. 75, 27–44.
Nguyen, V.T., Chan, W.H.R., Nguyen, H.H., 2018. Numerical investigation of wake induced vibrations of cylinders in tandem arrangement at subcritical Reynolds numbers. Ocean Eng. 154, 341–356.
Paidoussis, M.P., Price, S.J., 1988. The mechanisms underlying flow-induced instabilities of cylinder arrays in cross-flow. J. Fluid Mech. 187, 45–59.
Parkinson, G.V., 1971. Wind-induced instability of structures. Phil. Trans. Roy. Soc. Lond. Math. Phys. Sci. 269 (1199), 395–413.
Patankar, S.V., 1980. Numerical Heat Transfer and Fluid Flow. McGraw-Hill, New York.
Price, S.J., Piperni, P., 1988. An investigation of the effect of mechanical damping to alleviate wake-induced flutter of overhead power conductors. J. Fluid Struct. 2 (1), 53–71.
Sarpkaya, T., 2004. A critical review of the intrinsic nature of vortex-induced vibrations. J. Fluid Struct. 19 (4), 389–447.
Sarwar, M.W., Ishihara, T., 2010. Numerical study on suppression of vortex-induced vibrations of box girder bridge section by aerodynamic countermeasures. J. Wind Eng. Ind. Aerod. 98 (12), 701–711.
Simiu, E., Scanlan, R.H., 1996. Wind Effects on Structures, third ed. Wiley, New York.
Simpson, A., 1971. Wake induced flutter of circular cylinders: mechanical aspects. Aeronaut. Q. 22 (2), 101–118.
Smagorinsky, J., 1963. General circulation experiments with the primitive equations: I. The basic experiment. Mon. Weather Rev. 91 (3), 99–164.
Weaver, J., 1959. Experimental Investigation of Wind-Induced Vibrations in Antenna Members (No. GR-75-4). Massachusetts Institute of Technology: Lincoln Laboratory.
Williamson, C.H.K., Govardhan, R., 2004. Vortex-induced vibrations. Annu. Rev. Fluid Mech. 36, 413–455.
Williamson, C.H.K., Govardhan, R., 2008. A brief review of recent results in vortex-induced vibrations. J. Wind Eng. Ind. Aerod. 96 (6–7), 713–735.
Yao, W., Jaiman, R.K., 2019. Stability analysis of the wake-induced vibration of tandem circular and square cylinders. Nonlinear Dynam. 95 (1), 13–28.
Yagi, G., 2003. Wake Galloping of Tandem Circular Cylinders and Unsteady Pressure. Master thesis. Kochi University of Technology (In Japanese).
Yagi, T., Arima, M., Araki, S., Ogawa, S., Kosugi, T., Mohd Raizamzamani Md Zain, S., 2015. Investigation on wake-induced instabilities of parallel circular cylinders based on unsteady aerodynamic forces. In: Proc. Of 14th International Conference on Wind Engineering, Porto Alegre, Brazil, pp. 1–12.
Zdravkovich, M.M., 1981. Review and classification of various aerodynamic and hydrodynamic means for suppressing vortex shedding. J. Wind Eng. Ind. Aerod. 7 (2), 145–189.
Zhou, Y., Feng, S.X., Alam, M.M., Bai, H.L., 2009. Reynolds number effect on the wake of two staggered cylinders. Phys. Fluid. 21 (12), 125105.